energies

MDPI

Article

Lithofacies Characteristics, Depositional Environment and Sequence Stratigraphic Framework in the Saline Lacustrine Basin-A Case Study of the Eocene Low Member of Xingouzui Formation, Jianghan Basin, China

Xiaojie Fan [1], Yongchao Lu [1,*], Jingyu Zhang [2], Shiqiang Wu [3], Liang Zhang [3], Xiaojuan Du [3], Qinyu Cui [1] and Hao Wang [4]

1 School of Earth Resources, China University of Geoscience, Wuhan 430074, China
2 Centre for Marine Magnetism (CM2), Department of Ocean Science and Engineering, Southern University of Science and Technology, Shenzhen 518055, China
3 Exploration and Development Research Institute, Sinopec Jianghan Oilfield Company, Wuhan 430074, China
4 School of Marine Science and Technology, China University of Geoscience, Wuhan 430074, China
* Correspondence: luyc01@cug.edu.cn

Abstract: The Jianghan Basin is a lacustrine basin in central China developing multiple salt bearing deposits in the Eocene with the success of shale oil exploration in the Qianjiang Formation. The lower member of the Xingouzui Formation in the Chentuokou Depression has become another exploration target. However, rapid changes in lithofacies and strong sedimentary heterogeneity limit the exploration progress. This study aimed to explore the sequence division, lithofacies characteristics, and sedimentary environment using sedimentological, X-ray fluorescence (XRF) and X-ray diffraction (XRD) analyses. The sequence stratigraphic analysis indicates that the low member of the Xingouzui Formation is divided into two third-order sequences, namely SQ_1 and SQ_2, and four system tracts, including highstand systems tract (HST), lake expanding system tract (EST), early highstand system tract (EHST), and late highstand system tract (LHST). Moreover, a total of nine major lithofacies and five lithofacies associations (LA1-5) were identified. The organic geochemical data show that the laminated argillaceous dolomite in EST and EHST developed the best oil content with an average TOC of 1.18% and S_1 of 3.18 mg/g, The laminated argillaceous dolomite deposited in anoxic conditions with a humid climate, moderate salinity, and stratified deep waterbody is a favorable exploration facies for shale oil.

Keywords: sequence; lithofacies; sedimentary environment; shale oil; Jianghan Basin

Citation: Fan, X.; Lu, Y.; Zhang, J.; Wu, S.; Zhang, L.; Du, X.; Cui, Q.; Wang, H. Lithofacies Characteristics, Depositional Environment and Sequence Stratigraphic Framework in the Saline Lacustrine Basin-A Case Study of the Eocene Low Member of Xingouzui Formation, Jianghan Basin, China. *Energies* **2022**, *15*, 6235. https://doi.org/10.3390/en15176235

Academic Editor: Reza Rezaee

Received: 19 July 2022
Accepted: 22 August 2022
Published: 26 August 2022

1. Introduction

Sequence stratigraphy is an effective tool to research the basin filling process, distribution of sedimentary facies and predict the location of hydrocarbon reservoirs in passive continental margin environments [1–5]. However, this approach is restricted in the Cenozoic continental rift basins in China [2,6,7]. Continental lacustrine basins are susceptible to structure and climate [8–10] the sequence architecture is more complex, and difficult to predict. Paleoclimate change may as the primary influencing factor of the lacustrine basin's sedimentary process under stable structural conditions [8,9]. The high productivity and good preservation conditions of saline lacustrine basins provide a favorable place for organic matter accumulation, and they have accordingly been regarded as potential high-quality source rocks [11]. So, establishing the sequence stratigraphic framework of the saline lacustrine basin has great significance for the sedimentary environment and the prediction of the favorable zone.

Fine-grained sedimentary rock mainly composed of particles less than 62.5 μm [12,13] is both source rock and reservoir, containing abundant unconventional resources [14–16].

Previous studies suggest that laminated organic-rich fine-grained sedimentary rock is the most favorable exploration targets in shale oil exploration [9,17–19], but due to multiple depositional mechanisms the fine-grained sedimentary rock show strong heterogeneity with frequent lithofacies change [20,21]. Lithofacies, as the proxy for the paleoenvironment, is crucial for reconstructing the sedimentary environment and illuminating the process of organic matter enrichment, so the lithofacies characteristics in saline lacustrine basin still need detailed analysis.

The Jianghan Basin developed several salt bearing strata in the Eocene. Since the great success of the inter-salt shale oil reservoir in the Qiangjiang Formation [12–14] aroused interest in fine-grained sediments in saline lakes, recently, the Eocene low member of the Xinguozui Formation has emerged as a new field for inter-salt shale oil development in the Jianghan Basin [22]. The current focus of Xingouzui Formation research is primarily on organic geochemistry, reservoir characterization, and organic matter enrichment [22–27]. However, few studies have focused on the temporal and spatial evolution of lithofacies in sequence stratigraphic framework, the lithofacies characteristics and sedimentary environment in the saline lake still need further analysis.

The purpose of this paper is to explore the lithofacies evolution and sedimentary environment in different sequences and discuss lithofacies characteristics and oil content by sedimentology and geochemistry data. The results provide a new understanding of lithofacies characteristics and evolution in saline lakes.

2. Geological Setting

The Jianghan Basin is a Cretaceous–Paleogene petroliferous rift basin in the middle of the Yangtze Craton in Hubei Province, central China, spanning an area of about 28,000 km^2. The basin is bounded by Qinling-Dabie orogenic belt in the north, Dabie terrace and Edong fold-thrust belt in the east, Xuefeng uplift in the south, and Huangling anticline in the west [28–30], which can be further divided into five depressions and four uplifts including Jiangling Depression, Qianjiang Depression, Chentuokou Depression, Xiaoban Depression, Mianyang Depression and Yajiao-Xingou Uplift, Yuekou Uplift and Tonghaikou Uplift from west to east [22,24,28,31] (Figure 1). From Late Cretaceous to Paleogene, Jianghan Basin develops three stages of structural evolution, resulting in the formation of several collections of salt-bearing strata and source reservoir cap rock assemblages [29,30]. The Paleocene to Eocene sedimentary sequence from bottom to top includes Shashi Formation, Xingouzui Formation, Jingsha Formation, Qianjiang Formation, and Xingouzui Formation. Qianjiang Formation comprises the main source rocks, and in this study interval the lower Xingouzui Formation can be further subdivided into member III oil bed, clay interlayer, member II oil bed, and member I oil bed [29–33] (Figure 2A).

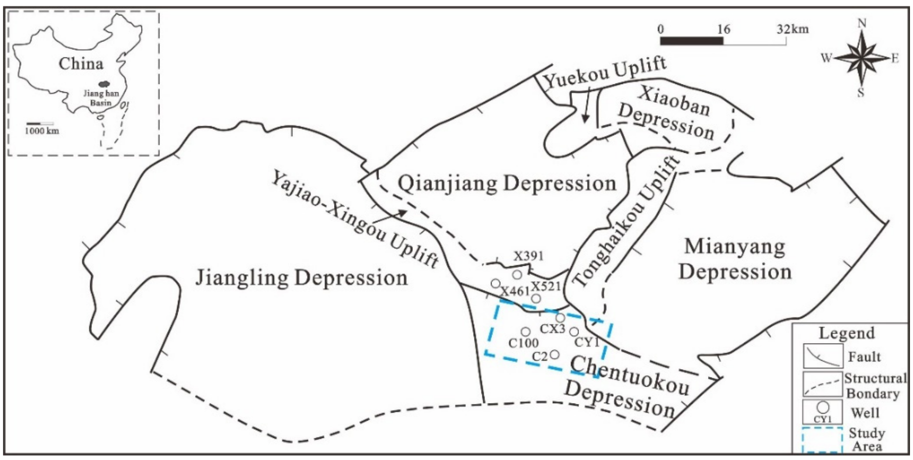

Figure 1. Generalized structural units map of the Jianghan Basin and research area modified from [24,27].

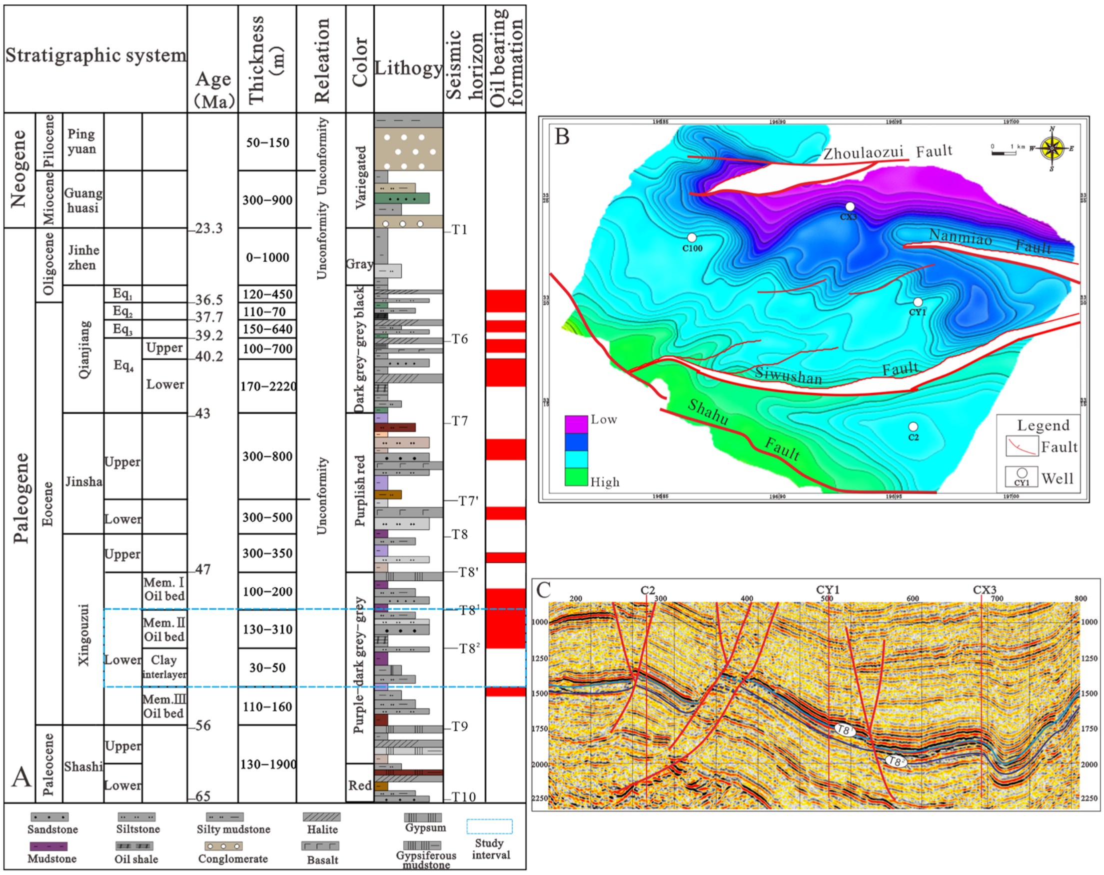

Figure 2. (**A**) Simplified Cenozoic stratigraphic column of Jianghan Basin modified from [31] age modified from [32] (**B**) Stratum thickness of the lower member of Xingouzui Formation in Chentuokou Depression (**C**) Seismic profile of well C2-CY1-CX3 in the Chentuokou Depression.

The Chentuokou Depression study area covers approximately 1500 km^2, as a typical half-graben depression in the southeast of the Jianghan Basin. Chentuokou Depression is adjacent to Jiangling Depression in the west and Tongshan Xianning fault-fold belt in the east, and bounded by Zhoulaozui fault and Shahu fault in the north and south, respectively (Figure 2A). The multiplied fault developed in the Chentuokou Depression has made the stratum thickness gradually thinner from north to south. As the exploration layer, the lithology of lower Xingouzui Formation comprises argillaceous dolomite, dolomitic mudstone, glauberite, and argillaceous siltstone, and industrial oil flow have been found in the argillaceous dolomite.

3. Materials and Methods

This study combined detailed sedimentological with geochemical analyses on the basis of a high-quality drill core of the well CY1. A total of 60 samples well collected from well CY1, including 35 dolomite samples, 18 mudstone samples, 4 siltstone samples and 3 glauberite samples.

All the samples were analyzed for TOC, rock pyrolysis, and XRD. Some samples were selected for scanning electron microscopy (SEM) and portable magnetic susceptibility. X-ray fluorescence (XRF) analysis was carried out for the entire study interval (130 m).

The TOC analysis was measured using a LECO CS–230. Prior to the experiment, all the samples were pulverized into granules with a particle diameter of less than 100 mesh. After that, inorganic carbon was removed using diluted hydrochloric acid (HCl) with a concentration of 10%. The rest of samples were rinsed, dried, reweighed, and then pyrolyzed at high temperatures. The test following the standards of GB/T19145-2003 [34].

The rock pyrolysis analysis was measured using an OGE-V1, where the sample was crushed into powder with a particle size of 0.07 mm–0.15 mm. The sample was heated to 600 °C at a rate of 25 °C/min under a helium environment with a purity greater than 99%. Then, the free hydrocarbons S_1, hydrocarbons cracked from kerogen S_2, and other pyrolytic parameters were obtained. The experimental utilized the standards for GB/T18602-2012.

XRD analysis was measured using a D/max-2600/pc X-ray diffractometer, and Cu Kα radiation at a scanning rate of 2°/min at 40 kV and 40 Ma with the testing angle ranging from 5° to 90°. The experimental utilized the standards for SY/T5163-2010 [35].

The selected samples were also studied for crystal size and morphology using a FEIQUANTA250 scanning electron microscope (SEM)

Magnetic susceptibility (MS) was measured using a Portable magnetic susceptibility SM-30. At the scanning mode, the interval between each scanning point is <15 cm, and the recording time is 30 s/per point.

X-ray fluorescence (XRF) was measured using Niton XL2, where the interval between each scanning point was less than 10 cm, and the recording time was 60 s/point. The measurement and recording are the count per second (CPS) value, which is automatically converted to parts per million (PPM) by the instrument. All the experiments were completed in the Jianghan Oilfield Research Institute.

4. Results

4.1. Lithofacies Description

Based on the sedimentological observation and mineralogy composition, we divided lithofacies by lithology and sedimentary structure. Four major lithologies, namely dolomite, mudstone, glauberite, and gypsum, can be identified in the low member of the Xingouzui Formation. We distinguish bedded and laminated structure by the thickness of single lamina. Hence, if the thickness of single lamina (e.g., dolomitic, argillaceous, glauberite) is less than 2 mm, it can be seen as laminated structure otherwise bedded structure. A total of nine major lithofacies can be identified in the low member of the Xingouzui Formation (Table 1, Figure 3).

Table 1. Characteristic of different lithofacies.

Lithology	Color	Structure	Characteristic	Sedimentary Environment
Argillaceous dolomite	Gray white	Massive	Homogeneous compositions	Shallow lake
	Gray brown	Bedded	Yellow dolomitic layers are interbedded with white glauberite layer	Semi deep lake
	Gray black	Laminated	Continuous morphology of yellow dolomitic lamina and black argillaceous lamina	Deep lake
Dolomitic mudstone	Dark gray	Bedded	Bedded dolomitic component Weaken upward	Deep lake
Silty mudstone	Gray brown		Yellow silty component distributed on argillaceous matrix	Semi deep lake
Glauberite mudstone	Dark gray	Bedded	Layered coarse-grained glauberite distributed on argillaceous matrix	Semi deep lake
argillaceous glauberite	Dark gray	Laminated	Fine-grained glauberite lamina interbedded with argillaceous lamina	Shallow lake
Glauberite	Gray white		With a dense arrangement of powdered glauberite crystals	Shallow lake
Gypsum	White		Gypsum agglomerate together to form larger clusters	Shallow lake

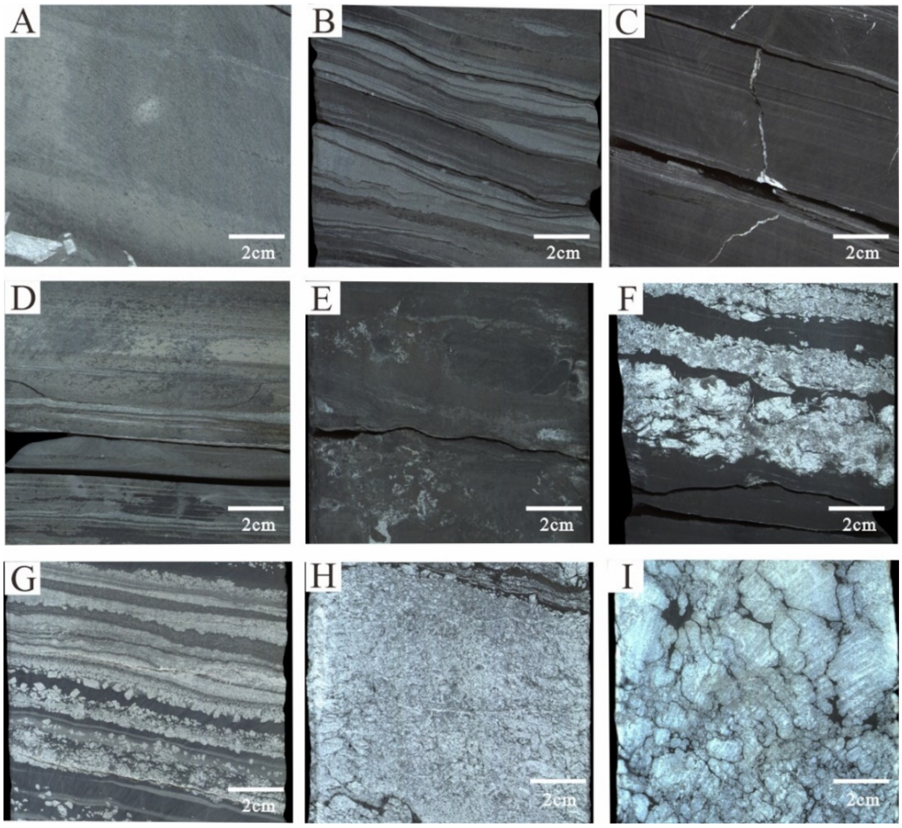

Figure 3. Main lithofacies characteristics of the lower member of Xingouzui Formation (**A**) Massive argillaceous dolomite, well CY1, 2647.83 m (**B**) Bedded argillaceous dolomite, well CY1, 2702.00 m (**C**) Laminated argillaceous dolomite well CY1, 2704.69 m (**D**) Bedded dolomitic mudstone, well CY1, 2635.70 m (**E**) Silty mudstone, well CY1, 2719.30 m (**F**) Glauberite mudstone, well CY1, 2725.30 m (**G**) Laminated argillaceous glauberite, well CY1, 2754.50 m (**H**) Glauberite, well CY1, 2677.4 m (**I**) Gypsum, well CY1, 2638.40 m.

Due to frequent changes in salinity and water depth, several salinization and desalination assembly have been found in the lowest member of the Xingouzui Formation. It can be further classified into five lithofacies associations (LA1-5) based on the vertical superposition of lithofacies (Figure 4).

LA1: Laminated glauberite mudstone + massive argillaceous dolomite, developed mostly in the clay interlayer and member III oil bed. The thickness of glauberite mudstone is greater than dolomite, white glauberite crystals are placed on the argillaceous matrix in the direction of powder-thin crystal laminae. The salinity gradually decreases from the bottom to the top, reflecting the shallow deposit.

LA2: Laminated argillaceous glauberite + Laminated argillaceous dolomite + Laminated dolomitic mudstone, the glauberite crystal is in the form of powder crystal laminae, the argillaceous dolomite has yellow layered, wavy, and lenticular bedding structure, and the dolomitic laminae and argillaceous laminae are seen in the dolomitic mudstone. This reflects a desalination process in which the salinity is dropping and the hydrodynamic force is waning

LA3: Massive argillaceous dolomite + glauberite, formed primarily in the bottom of the member III oil bed. This illustrates the steady rise in salinity until glauberite deposition takes place in a salinization combination.

LA4: Massive argillaceous dolomite + laminated dolomitic mudstone, yellow dolomitic laminae, and white glauberite laminae can be seen in the mudstone, which is primarily developed in the middle of member III oil bed, and the salinity is relatively low.

LA5: Argillaceous gypsum + bedded dolomitic mudstone + gypsiferous mudstone, primarily in the top of member III oil bed, reflect a desalination combination. The deposited salt minerals are gypsum rather than glauberite, indicating that the salinity is reduced.

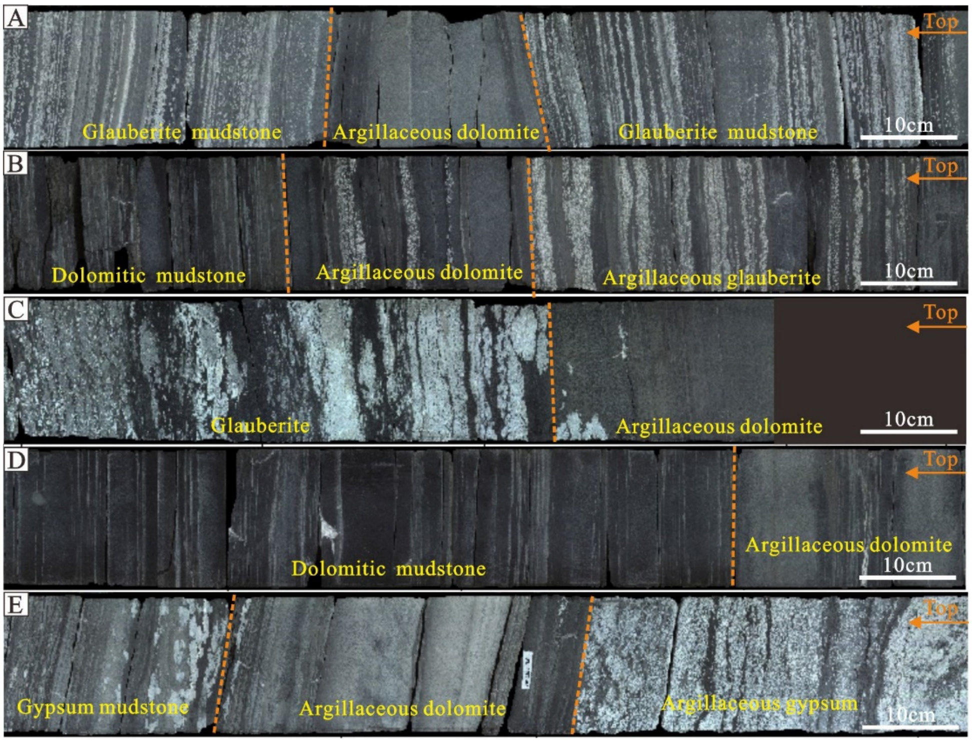

Figure 4. Lithofacies associations (**A**) LA1 well CY1 2754.6–2755.6 m (**B**) LA2 well CY1 2736.6–2737.6 m (**C**) LA3 well CY1 2708.5–2709 m (**D**) LA4 well CY1 2722–2732 m (**E**) LA5 well CY1 2648–2649 m.

4.2. Mineralogy Characteristics

The XRD results of different lithofacies are shown in Figure 5 and Table 2. The argillaceous dolomite has a high content of dolomite ranging from 34.5% to 87.3% and medium content of silicate minerals (quartz + feldspar) ranging from 7.8% to 39.6%, low clay minerals content ranging from 0.8% to 25.3%. The dolomitic mudstone has a similar content in dolomite, silicate, and clay minerals ranging from 13.7% to 43.7%, 7.1% to 25.5%, and 9.6% to 37.4% respectively. In silty mudstone, the average contents of clay minerals, quartz, feldspar, and dolomite are 38.5%, 16.3%, 15.8%, and 12.1%. The average content of clay minerals, quartz, feldspar, and dolomite in argillaceous siltstone is 18.1%, 21.3%, 34.6%, and 22.5% respectively. For the glauberite, there was an average content of 68.3% glauberite, followed by anhydrite, with an average content of 9.7%, and a small amount of feldspar and quartz.

As the main minerals in the study interval, it is important to discuss the origin of dolomite and glauberite. The SEM analyses show that the dolomite crystals are generally less than 2 μm in size, and dolomite crystals are mainly automorphic with little terrigenous input (Figure 6A–C). The morphology of dolomite which is similar with other studies in same period (e.g., Jianghan basin [36], Nanyang basin [37]). During the study interval, the dolomite samples have undergone little diagenetic alteration, showing characteristics of authigenic carbonates. The glauberite appears with a dense arrangement of powdered crystals on the core samples and presents the radiated aggregate on SEM (Figure 6D,E). Rhythmic features are obviously deposited directly in the lake.

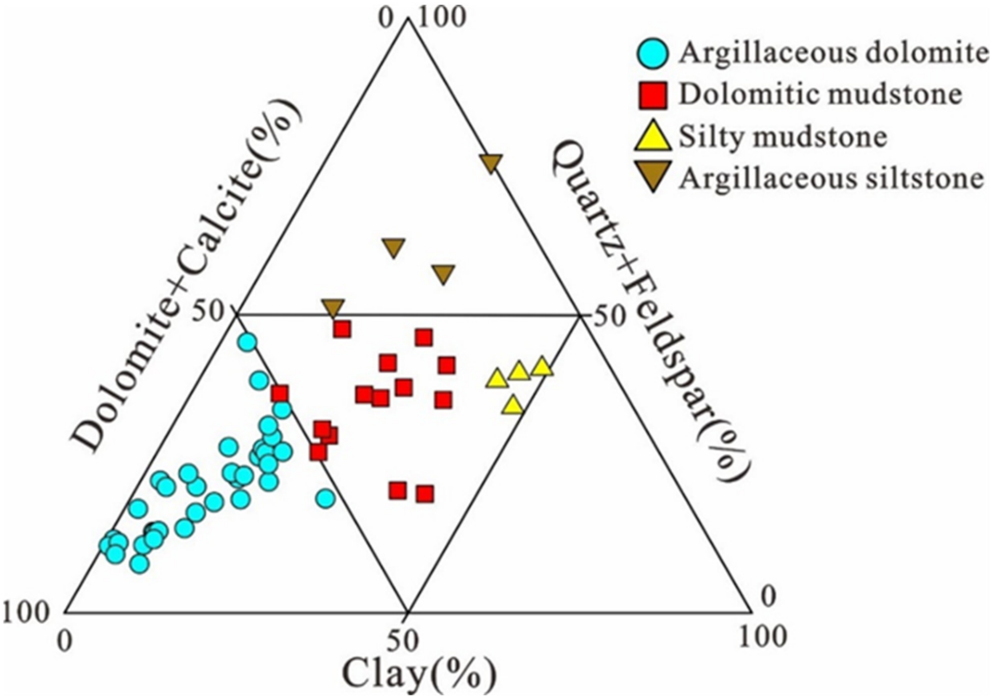

Figure 5. Ternary diagram of the lower member of the Xingouzui Formation.

Table 2. Mineral contents of different lithofacies.

	Mineral Composition							
	Clay (%)	**Quartz (%)**	**Feldspar (%)**	**Pyrite (%)**	**Calcite (%)**	**Dolomite (%)**	**Anhydrite (%)**	**Glauberite (%)**
Massive argillaceous dolomite	1.5–25.3 (9.9)	2.9–18.4 (7.9)	7.3–21.2 (13.2)	0.9–5 (3.7)	4–17.3 (13)	44.1–85 (56.9)	0.8–22 (5.1)	1.0–4.3 (2.4)
Bedded argillaceous dolomite	5.8–16.2 (11.6)	3.0–11.3 (6.0)	5.2–22.7 (14.8)	1.3–7.6 (4.3)	4.3–14.0 (8.6)	34.5–83.8 (53.7)	1.3–14.9 (5.4)	2.2–7.1 (4.4)
Laminated argillaceous dolomite	0.8–13.5 (6.4)	0.9–14.9 (4.6)	6.9–17.6 (11.1)	1.8–7.5 (4.9)	5.9–8.8 (7.5)	46.0–87.3 (70.3)	0.4–12.6 (2.7)	1.2–6.6 (3.9)
Massive dolomitic mudstone	9.6–34.4 (23.0)	6.7–20.9 (12.6)	7.8–25.5 (18.4)	2.6–6.6 (4.2)	17–20.6 (18.8)	16.0–37.4 (24.0)	1.3–22.9 (9.0)	1.6–8.5 (5.1)
Bedded dolomitic mudstone	15.5–21.6 (19.6)	10.5–19.6 (14.3)	10.6–24.9 (16.8)	3.6–5.6 (4.6)	14.5	31.0–40.7 (37.3)	1.1–5.7 (3.1)	-
Laminated dolomitic mudstone	19.8–37.4 (28.4)	3.5–16.0 (11.1)	7.1–21.1 (16.5)	3.5–7.3 (5.8)	5.5	13.7–33.1 (22.7)	1.1–6.8 (3.9)	1.3–10.9 (6.1)
Silty mudstone	36.9–41.2 (38.5)	13.5–18.3 (16.3)	10.6–20.8 (15.8)	5.0–9.2 (7.4)	-	8.4–15.4 (12.1)	1.9–5.5 (3.2)	2.3–10.0 (5.2)
Argillaceous siltstone	13.2–22.0 (18.1)	13.5–29.3 (21.3)	32.3–39.9 (34.6)	4.0–6.8 (5.0)	-	13.0–34.8 (22.5)	1.0–7.1 (4.2)	1.3–10.9 (6.1)
Glauberite	3.5–8.6 (5.8)	0.7–4.4 (2.7)	8.6–10.7 (6.4)	5.2	-	15.9	6.0–16.9 (9.7)	61.2–77.2 (68.3)

Note: 1.5–25.3 = Min–Max, (9.9) = Average.

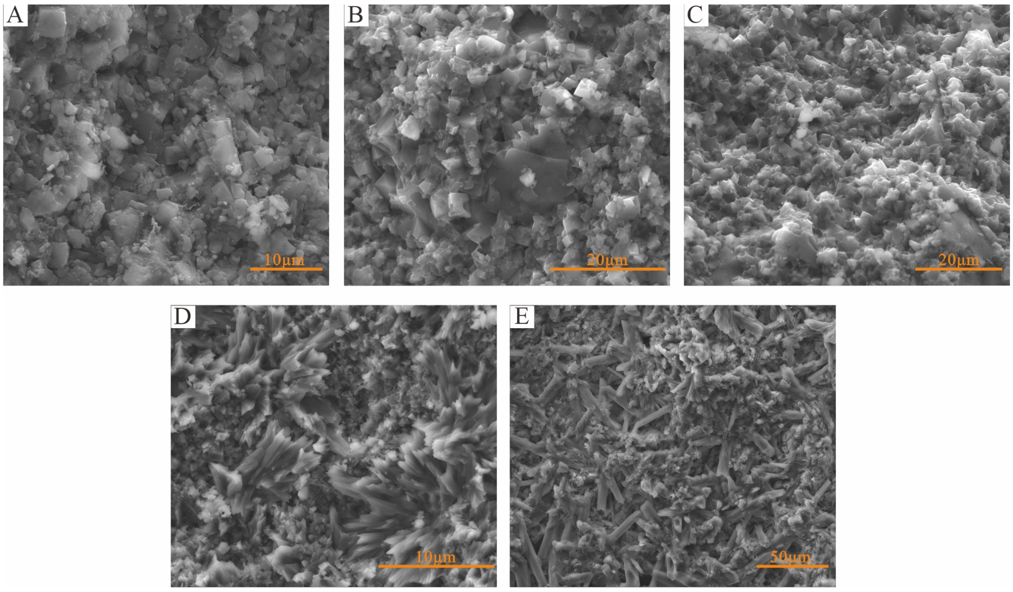

Figure 6. Scanning electron microscope (SEM) images of the lower member of Xingouzui Formation (**A**–**C**) Dolomite well CY1, 2701.04 m, 2702.86 m, 2709.73 m (**D**,**E**) Glauberite well CY1, 2700.65 m, 2706.09 m.

4.3. Hydrocarbon Generation Potential

Organic matter abundance is usually characterized by total organic carbon content (TOC), rock pyrolysis parameters free hydrocarbon (S_1), hydrocarbons cracked from kerogen (S_2), hydrocarbon generation potential ($S_1 + S_2$), oil saturation index (OSI = S_1/TOC × 100) [22–24,38]. Organic matter in the lower member of Xinguozui Formation is enriched in argillaceous dolomite, which is dominated by type I and type II kerogen and in low maturity evolution stage [22–25].

Laminated argillaceous dolomite has the highest organic matter abundance. The TOC value of the 11 laminated argillaceous dolomite samples is distributed from 0.65% to 2.22%, with an average of 1.18%. S_1 of these samples are distributed from 1.85 mg/g to 7.19 mg/g, with an average of 3.08 mg/g. S_2 is distributed between 0.91% and 4.48%, with an average of 2.81% (Table 3). Massive argillaceous dolomite, bedded dolomitic mudstone, and glauberite appear to have low levels of organic matter. The average TOC for these lithofacies is less than 0.5%.

Table 3. Organic geochemical parameters of different lithofacies.

Lithofacies	TOC (%)	S_1 (mg/g)	S_2 (mg/g)	$S_1 + S_2$ (mg/g)	S_1/TOC × 100 (mg/g)
Massive argillaceous dolomite	0.17–0.85 (0.49)	0.06–1.56 (0.59)	0.08–0.98 (0.49)	0.14–2.01 (1.08)	41–295 (117)
Bedded argillaceous dolomite	0.35–1.38 (1.01)	0.14–1.34 (0.97)	0.20–3.91 (1.13)	0.34–5.99 (2.11)	48–193 (93)
Laminated argillaceous dolomite	0.65–2.22 (1.18)	1.85–7.19 (3.08)	0.91–4.48 (2.81)	2.86–11.67 (5.90)	115–445 (266)
Massive Dolomitic mudstone	0.17–2.69 (0.85)	0.09–2.32 (0.76)	0.13–2.8 (0.86)	0.22–5.15 (1.62)	52–110 (82)
Bedded Dolomitic mudstone	0.28–0.56 (0.43)	0.11–0.66 (0.32)	0.18–0.49 (0.35)	0.29–1.17 (0.67)	39–117 (68)
Laminated Dolomitic mudstone	0.46–1.8 (0.89)	0.10–2.08 (0.83)	0.11–3.37 (1.27)	0.21–5.45 (2.1)	14–117 (84)
Silty mudstone	0.34–1.61 (1.11)	0.10–2.61 (1.25)	0.13–3.16 (1.64)	0.23–5.77 (2.90)	29–102 (94)
Argillaceous siltstone	0.82–2.26 (1.33)	0.68–2.18 (1.49)	0.87–4.02 (2.02)	1.55–6.04 (3.51)	82–168 (113)
Glauberite	0.06–1.05 (0.43)	0.04–0.63 (0.24)	0.06–1.02 (0.39)	0.10–1.65 (1.9)	33–66 (53)

Note: 0.17–0.85 = Min–Max, (0.49) = Average.

5. Discussion

5.1. Sequence Stratigraphic Framework and Lithofacies Variation

The differences in mineral composition, lithology, and sedimentary structure can be expressed by lithofacies or lithofacies assembly. Similar lithofacies or lithofacies assembly are performed with the same sedimentary environment and similar organic matter abundance and reservoir properties [17]. Lake level affects lithofacies the relative lake level and sequence boundaries can be distinguished by the superposition connection of various lithofacies [7,39]. The third-order sequence boundary and system tract interface are identified through the superposition relationship of lithofacies assembly, lithologic catastrophe interface, and trend of logging (GR, Resistivity). Each system tract has developed different lithofacies and lithofacies assembly, suggesting variations sedimentary environment of the lacustrine basin in different periods.

At the top of the clay interlayer in well CY1, there is a clear abrupt change in the resistivity curve that can be contrasted throughout the entire research region as a third order sequence boundary, and the upward-declining amplitude of the GR curve at the top of the member II oil bed can be regarded as another third order sequence boundary. Hence, two third order sequences, SQ_1 and SQ_2, can be identified in the low Xinguozui Formation (Figure 7).

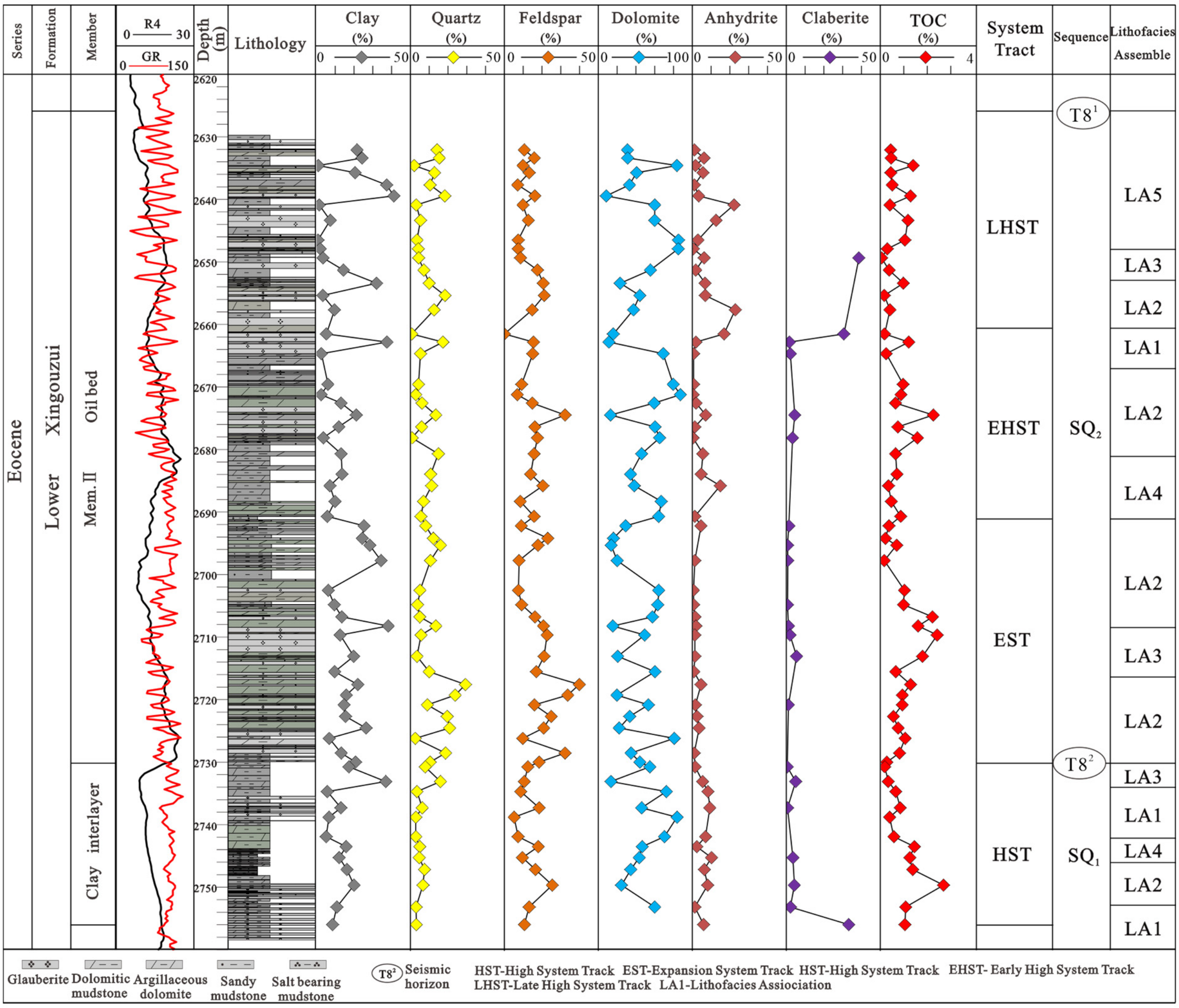

Figure 7. Sequence and lithofacies associations column of well CY1.

The classical sequence stratigraphic model consists a complete depositional sequence with a lowstand systems tract (LST), a transgressive systems tract (TST) and a highstand systems tract (HST) [2,4], In the lacustrine basin the TST is equal to the lake expanding system tract (EST) [40], due to the long shallow water period and large amount of evaporite the HST can be subdivided into early highstand system tract (EHST) and late highstand system tract (LHST). The lowstand system tract is absent because the study interval was deposited above the structural slope break [41] (Figure 2B,C). Hence, in this study, the systems tract interpretation follows EST-EHST-LHST in SQ_2.

Four major lithofacies assembly can be distinguished in SQ_1. Multiple LA1 can be observed at the bottom and as the salinity decreases upward the thickness of glauberite layer gradually decreases, to become LA2 and LA3. Here, the thickness of lithofacies associations which indicates a shallow water environment continues to increase from bottom to top. It is a highstand system tract (HST).

There are mainly two lithofacies assemblies at the bottom of SQ_2, several desalination combinations LA2 suggest an increasing depth of water, LA3 as an interlayer in the middle and the thickness of glauberite decreases upward transits to LA2 again and the occurrence of laminated silty mudstone may be related to intermittent rainfall. The thickness of lithofacies assemblage, as an indicator of deep water, gradually increases from bottom to top, suggesting that the lake is expanding and the water becomes deeper as a lake expanding system tract (EST).

Three lithofacies assembly can be identified in the middle of SQ_2, at the bottom, where the water is shallow and subject to strong hydrodynamic forces. In this assembly, LA4 is mostly deposited, followed by LA2 from a number of desalination combinations in the center, and LA1 as salinity levels rise. The water depth went through a shallow-deep-shallow cycle from bottom to top, which is an early highstand system tract (EHST).

The deposited salt minerals shifted from glauberite to gypsum from bottom to top when salinity decreased at the top of SQ_2, and lithofacies assemblies appeared in the form of LA2-LA3-LA5, it indicates that the lake is shrinking and the water depth is gradually shallowing, which is a late highstand system tract (LHST).

As the lake in the Chentuokou Depression deepened from south to north during the deposited period of the lower member of the Xingouzui Formation, the mineral composition and particle size of the sediments likewise altered according to the distance from the provenance. The lake is shallow during the HST period of SQ_1, and well C2 close to the provenance is composed of sandy mudstone + mudstone. With the salinity increases, well CY1 is glauberite + argillaceous dolomite, and well CX3 at the deepest is deposited with gypsiferous mudstone (Figure 8).

The lake expands, the terrigenous input declines, and evaporation rises during the EST period of SQ_2. Gypsiferous mudstone, argillaceous dolomite, glauberite, and gypsum are all formed as a result of the progressive rise in salinity from north to south. Intermittent rainfall may alter the top of EST. Provenance supply is abundant, siltstone and argillaceous siltstone are developed in well C2, and laminated silty mudstone transitions to well CY1 with the loss of northern transportation capacity.

Lake drops during the EHST period, salinity increases, and well C2 develops gypsiferous mudstone. Meanwhile, well CY1 transitions from dolomitic mudstone to glauberite to the north, well CX3 transitions from gypsiferous mudstone to gypsum rock toward the deep lake. Lake drops further, evaporation, and salinity all decrease throughout the LHST era. In well C2, gypsum and silty mudstone have developed. Gypsum, glauberite, and bedded dolomitic mudstone are mostly formed in well CY1, while well CX3 has a significant portion of dolomitic mudstone.

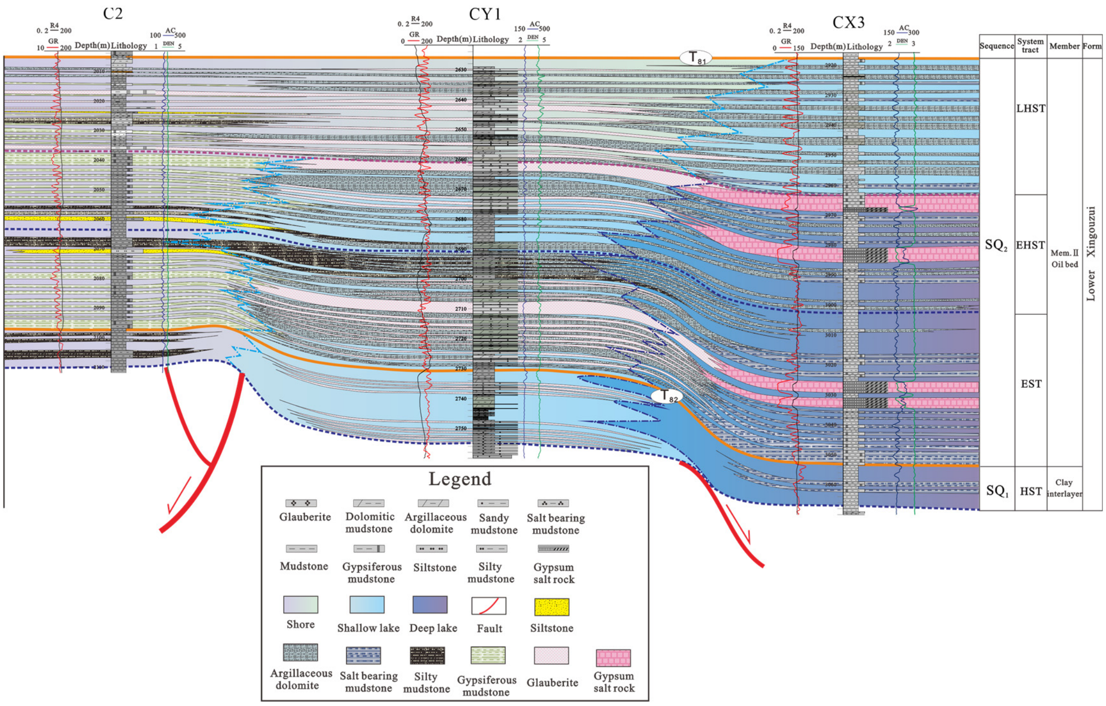

Figure 8. Cross well of C2-CY1-CX3 in Chentuokou Depression location see in Figure 2.

5.2. Organic Matter Abundance of Different Lithofacies

Organic matter abundance, reservoir, liquidity, and compressibility as the basic parameters to evaluate the potential of unconventional resources are crucial in exploration [42].

Among them, organic matter abundance as the material basis is the primary consideration, which is influenced by variations in the sedimentary environment and mineral composition.

In the saline lake if TOC > 0.6 can be considered a good source rock [24,25]. Laminated argillaceous dolomite has the highest organic matter abundance, with the average TOC and S_1 of 1.18% and 3.08 mg/g, followed by bedded argillaceous dolomite, with the average TOC and S_1 of 1.01% and 0.97 mg/g respectively, massive argillaceous dolomite and dolomitic mudstone have poor oil content. Despite having significant oil content, argillaceous siltstone and silty mudstone are not mentioned here due to a limitation of samples. Vermicular scattered and laminated alginite are detected in the argillaceous dolomite in Well C100 [25]. In addition, free oil molecules fill the dolomite matrix pores and laminar fractures in well CY1 [24], both indicating that argillaceous dolomite has excellent hydrocarbon potential for oil generation (Figures 9 and 10).

5.3. Sedimentary Environment

Rapid climate change has a significant impact on the lacustrine basin, resulting in the strong heterogeneity of sediments. Portable XRF has the advantages of continuous data and rapid and nondestructive testing, which have been widely utilized to get the geochemical parameters [43–46], XRF data obtained the contents of 17 elements, such as Si, Al, CA, Mg, Fe, Rb, and Sr, with 1963 data points for each element.

Magnetic susceptibility is an effective proxy of paleoenvironmental which can assess the changes in magnetic materials in sedimentary environments [45]. A total of 1532 susceptibility scanning points were obtained, and the minimum and maximum values were distributed between 0.003 and 0.069 SI. High resolution of XRF data and magnetic susceptibility were used to reconstruct the sedimentary environment.

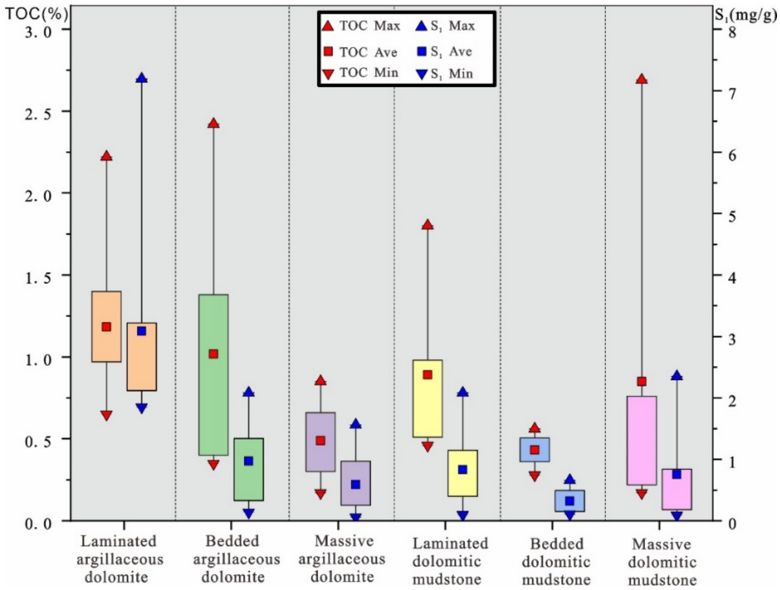

Figure 9. TOC and S_1 box diagram of different lithofacies in the lower member of Xingouzui Formation.

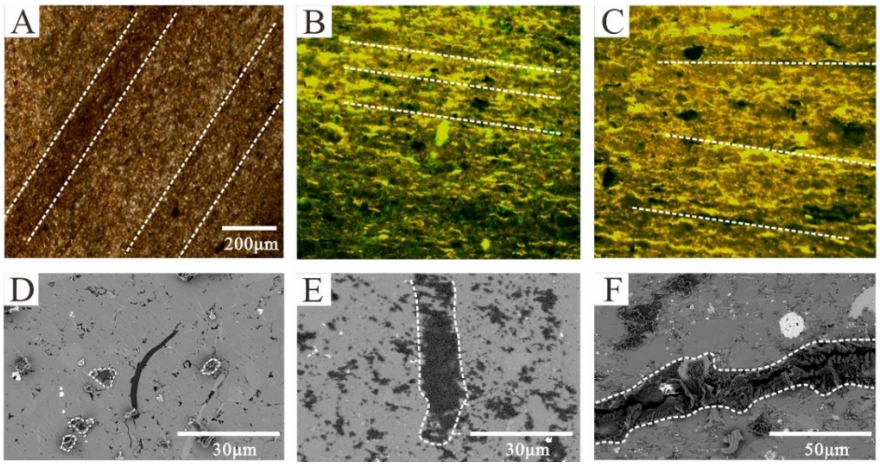

Figure 10. Microscopic characteristics of laminated argillaceous dolomite (**A**) Dolomite lamina well CY1 2682.89 m after [24] (**B**,**C**) Laminated alginite well C100 2156.9 m 2191.05 m after [25] (**D**,**E**) Oil molecules fill the pores of dolomite matrix well CY1 after [23] (**F**) Laminar fractures are developed and filled with oil molecules well CY1 after [23] Dotted white lines indicate lamina in (**A**–**C**) and precipitated oil in (**D**,**E**).

5.3.1. Redox Conditions

The degree of pyritization (DOP) is a common proxy to estimate redox conditions. Since the ratio of iron to total iron in pyrite is similar, DOP_T (DOP_T = (55.85/64.16) × S/Fe) can be used to approximately replace DOP [46–49], (S_1 + S_2)/TOC also widely used to indicate the redox conditions in fine-grained sedimentary rocks [50,51]; both of them have a positive correlation with redox conditions.

The study interval is anoxic, and during the LHST period redox conditions change frequently, which shows the interactive deposition of gypsum and mudstone (Figure 11).

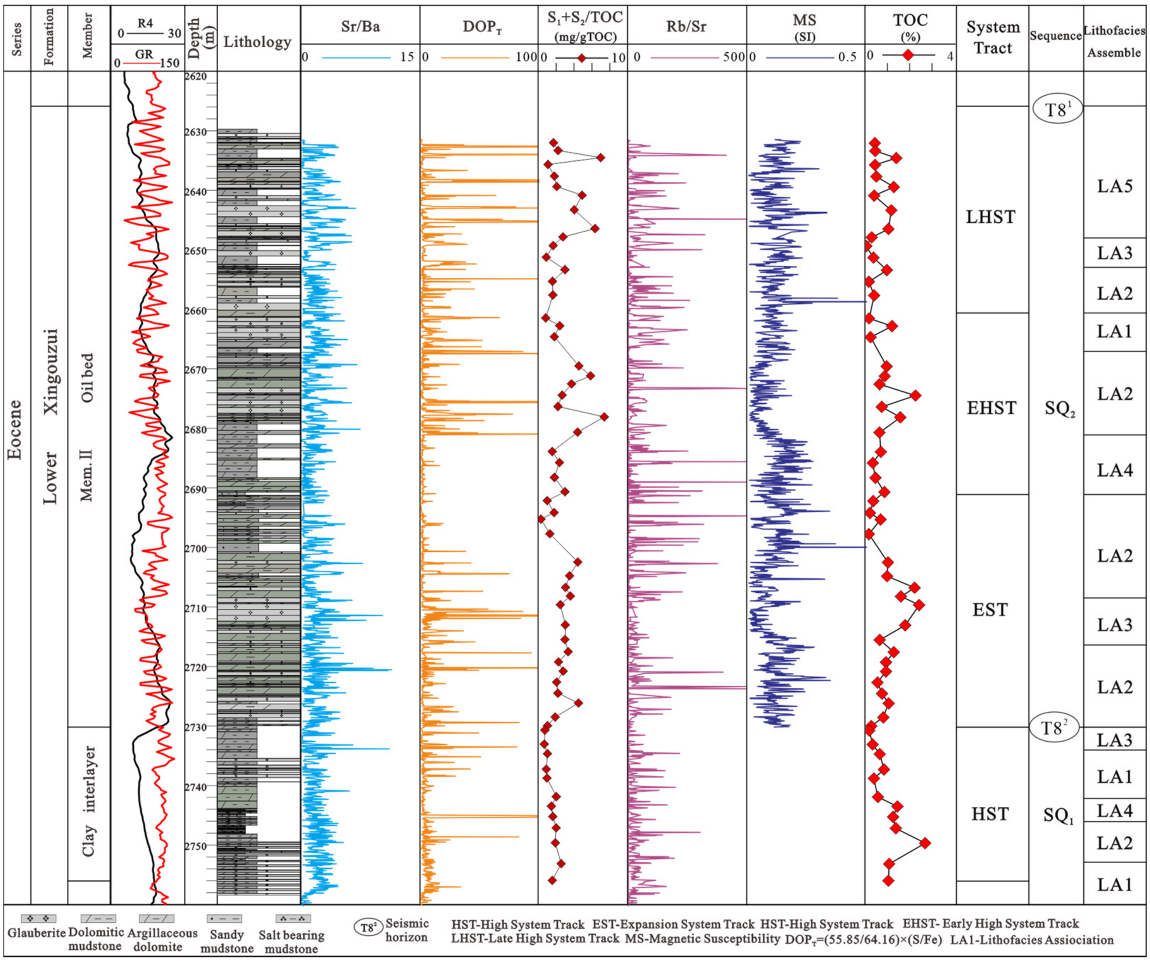

Figure 11. Geochemical parameters of lower member of Xingouzui Formation.

5.3.2. Paleosalinity

A reliable indicator of paleosalinity is the Sr/Ba ratios [52]. Large Sr/Ba ratios typically indicate a salty environment. Multiple salinity fluctuations occurred during the period of lower member Xingouzui Formation deposition, which was reflected in the frequent appearance and disappearance of evaporite rocks as glauberite and gypsum. Paleosalinity was higher in the clay interlayer and much lower when gypsum was deposited on the top of the member II oil bed.

5.3.3. Paleoclimate Significance

(1). Can Paleocene-Eocene Thermal Maximum (PETM) be identified in the depositional period of low Xingouzui Formation?

The global climate was warm during the late Paleocene to the early Eocene. During this period, the Paleocene-Eocene Thermal Maximum (PETM) has attracted the most attention [53–55]. It is a geological transient period with significant changes in global climate and ecological environment [56,57]. During this period, a huge amount of light carbon quickly integrated into the ocean atmosphere system in a short time, resulting in rapid global warming and seawater hypoxia. The carbon release process is similar to burning fossil fuels [58]. Therefore, this event provides an ideal model for understanding today's rapid global warming [54,57]. Based on the evidence of radioisotope, paleomagnetic, paleontology, carbonate isotope excursion [32,36,57,59], some scholars have identified PETM events in the Xingouzui and Yangxi formation of the early Eocene in the Jianghan Basin The specific performance is that the rainfall suddenly increases with humid climate. The abundant rainfall and humid climate provide good conditions for the nutrition of forest systems and lakes [32,36,57,59,60]. If this event can be identified in the lower Xingouzui Formation, it can provide different explanations for the organic matter enrichment in this area. Through the comparison of strata, lithology, and mineral composition, this study suggests that the study interval is more likely to be deposited after the PETM event, on the basis of the following: 1. During the PETM period, the carbonate minerals deposited in Jianghan Basin due to humid climate are mainly calcite and calcite/dolomite > 1, while calcite rarely appears in study interval, i.e., only 14 of the 60 samples contain calcite, with an average of only 10.9%, and the calcite/dolomite ratio is far less than 1. 2. A large number of terrigenous clasts such as quartz, feldspar and other minerals carried by enhanced rainfall did not appear on a large scale in study interval, dolomite still dominates. 3. Evaporite rocks, such as glauberite and gypsum, which widely appear from top to bottom also indicate a relatively arid climate.

(2). Paleoclimate change

The increased terrigenous input due to the humid climate in lakes dominated by exogenous magnetic minerals may lead to high magnetic susceptibility [45]. Rb/Sr ratio can be used as a reliable index of chemical weathering intensity of fine-grained sediments in lakes. The low value of Rb/Sr has low chemical weathering intensity and a relatively dry climate [61]. The variation trends of magnetic susceptibility and Rb/Sr in the lower member of the Xingouzui Formation both show three increasing and decreasing trends from the bottom to the top, with obvious cyclicity, indicating that the paleoclimate fluctuated frequently between drought and humidity during this period.

5.3.4. Sedimentary Model

The lithofacies assemblies and oil content differ as a result of the sedimentary environment changing in a different sequence. During the HST period of SQ_1, the lake gradually became shallower, the redox conditions were weak, the climate was relatively dry, and the salinity changed frequently. When the salinity increased, the thickness of glauberite in each lithofacies associations was relatively large. When the salinity decreased, argillaceous dolomite and dolomitic mudstone were the main sediments, and the TOC content gradually decreased upward, which resulted in salinity stratified water with strong evaporation.

During the EST period of SQ_2, the water body gradually became deeper, which is an anoxic condition. The climate circulates between humidity and drought. During the transition from glauberite + massive argillaceous dolomite to bedded/laminated argillaceous dolomite, TOC and S_1 increase to the maximum, suggesting that anoxic conditions with a humid climate, and moderate salinity are more conducive to the enrichment of organic matter.

During the EHST period, the water became shallow slowly, and the salinity decreased. The climate also circulates between humidity and drought. The TOC tendency was similar to the EST that laminated argillaceous dolomite in the LA2, having a higher TOC value.

During the LHST period, the lake level declined further, and the salinity was lower than before. Such a phenomenon was dominated by the interactive deposition of LA5. Gypsiferous mudstone and bedded dolomitic mudstone were deposited at the disturbed saline waterbody.

6. Conclusions

We combined detailed sedimentological with geochemical analyses of the early Eocene lower member of the Xingouzui Formation in the Chentuokou Depression, Jianghan Basin. The lithofacies characteristics and sedimentary environment within the sequence framework are clarified. The lower member of the Xingouzui Formation can be divided into two third sequences, SQ_1, $SQ_{2,}$ and four system tracts, highstand system tract (HST), lake expanding system tract (EST), early highstand system tract (EHST), and late highstand system tract (LHST). Nine major lithofacies and five lithofacies assemblies were developed in different system tracts.

The study interval considered deposition after the PETM, when the climate fluctuates between drought and humidity. Laminated argillaceous dolomite lithofacies deposited in anoxic conditions with a humid climate, and moderate salinity is more conducive to the enrichment of organic matter, leading to relatively high TOC and S_1 values. The bedded or laminated argillaceous dolomite developed in EST and EHST are the most favorable target lithofacies for shale oil exploration.

Author Contributions: X.F.: conceptualization, methodology, writing—original draft preparation; Y.L.: supervision, writing—review and editing, validation; J.Z.: methodology, writing—review and editing; S.W.: validation; L.Z.: resources, validation; X.D.: data curation, validation; Q.C.: visualization; H.W.: visualization. All authors have read and agreed to the published version of the manuscript.

Funding: This research was funded by Formation and enrichment mechanism of shale oil in Xingouzui Formation, Chentuokou depression Jianghan basin (31400032-21-ZC0613-0002) of the Jianghan Oilfield Research Institute Sinopec Corp, and China Scholarship Council (CSC).

Data Availability Statement: The data presented in this study are available on request from the corresponding author.

Conflicts of Interest: The authors declare no conflict of interest.

References

1. Vail, P.R., Jr.; Thomposons, S. Global-cycles of relative changes of sea level. *AAPG Memoir* **1977**, *83*, 469–472.
2. Feng, Y.; Li, S.; Lu, Y. Sequence stratigraphy and architectural variability in Late Eocene lacustrine strata of the Dongying Depression, Bohai Bay Basin, Eastern China—ScienceDirect. *Sediment. Geol* **2013**, *295*, 1–26. [CrossRef]
3. Wagoner, J.C.V.; Mitchum, R.M.; Campion, K.M.; Rahmanian, V.D. Siliciclastic Sequence Stratigraphy in Well Logs, Cores, and Outcrops: Concepts for High-Resolution Correlation of Time and Fades. *Geol. Mag.* **1990**, *7*, 55.
4. Catuneanu, O.; Abreu, V.; Bhattacharya, J.P.; Blum, M.D.; Dalrymple, R.W.; Eriksson, P.G.; Fielding, C.R.; Fisher, W.L.; Galloway, W.E.; Gibling, M.R. Towards the standardization of sequence stratigraphy. *Earth Sci. Rev.* **2009**, *92*, 1–33. [CrossRef]
5. Wood, J. Chronostratigraphy and tectonostratigraphy of the Columbus Basin, eastern offshore Trinidad. *AAPG Bull.* **2000**, *84*, 1905–1928.
6. Shanley, K.W.; Mccabe, P.J. Perspectives on the sequence stratigraphy of continental strata. *AAPG Bull.* **1994**, *78*, 544–568.
7. Wu, J.; Jiang, Z.; Wang, X. Sequence stratigraphy characteristics of lacurine fine-grained sedimentary rocks: A case study of the upper fourth member of Paleogene Shahejie Formation, Dongying Sag, Bohai Bay Basin. *Nat. Gas Geosci.* **2018**, *29*, 199–210, (In Chinese with English abstract).
8. Zhu, H.; Zeng, H.; Liu, K. A quantitative simulation study of asymmetrical tectonic subsidence control on non-synchronous sequence stacking patterns of Eocene lacustrine sediments in Bohai Bay Basin, China - ScienceDirect. *Sediment. Geol.* **2013**, *294*, 328–341. [CrossRef]
9. Ma, Y.; Fan, M.; Lu, Y.; Liu, H.; Hao, Y.; Xie, Z.; Liu, Z.; Peng, L.; Du, X.; Hu, H. Climate-driven paleolimnological change controls lacustrine mudstone depositional process and organic matter accumulation: Constraints from lithofacies and geochemical studies in the Zhanhua Depression, eastern China. *Int. J. Coal Geol.* **2016**, *167*, 103–118. [CrossRef]
10. Keighley, D.; Flint, S.; Howell, J.; Moscariello, A. Sequence Stratigraphy in Lacustrine Basins: A Model for Part of the Green River Formation (Eocene), Southwest Uinta Basin, Utah, USA. *J. Sediment. Res.* **2003**, *73*, 987–1006. [CrossRef]
11. Zou, C.; Zhu, R.; Chen, Z.; Ogg, J.G.; Wu, S.; Dong, D.; Qiu, Z.; Wang, Y.; Wang, L.; Lin, S.; et al. Organic-matter-rich shales of China. *Earth Sci. Rev.* **2019**, *189*, 51–78. [CrossRef]
12. Picard, M.D. Classification of fine-grained sedimentary rocks. *J. Sediment. Res.* **1971**, *41*, 179–195.
13. Lazar, O.R.; Bohacs, K.M.; Macquaker, J.; Schieber, J.; Demko, T.M. Capturing Key Attributes of Fine-Grained Sedimentary Rocks in Outcrops, Cores, and Thin Sections: Nomenclature and Description Guidelines. *J. Sediment. Res.* **2015**, *85*, 230–246. [CrossRef]
14. Jia, C.; Zou, C.; Yang, Z.; Zhu, R.; Chen, Z. Significant progress of continental petroleum geological theory in basins of Central and Western China. *Pet. Explor. Dev.* **2018**, *45*, 573–588. [CrossRef]
15. Sun, L.; Zou, C.; Jia, A.; Wei, Y.; Guo, Z. Development characteristics and orientation of tight oil and gas in China. *Petrol. Explor. Dev.* **2019**, *46*, 1073–1087. [CrossRef]
16. Loucks, R.G.; Ruppel, S.C. Mississippian Barnett Shale: Lithofacies and depositional setting of a deep-water shale-gas succession in the Fort Worth Basin, Texas. *AAPG Bull.* **2007**, *91*, 579–601. [CrossRef]
17. Bai, C.; Yu, B.; Han, S.; Shen, Z. Characterization of lithofacies in shale oil reservoirs of a lacustrine basin in eastern China: Implications for oil accumulation. *J. Petrol. Sci. Eng.* **2020**, *195*, 107907. [CrossRef]
18. Su, A.; Chen, H.; Zhao, J.; Feng, Y. Integrated fluid inclusion analysis and petrography constraints on the petroleum system evolution of the central and southern Biyang Sag, Nanxiang Basin, Eastern China. *Mar. Petrol. Geol.* **2020**, *118*, 104437. [CrossRef]

19. Zhao, X.; Zhou, L.; Pu, X.; Han, W.; Jin, F.; Xiao, D.; Shi, Z.; Deng, Y.; Zhang, W.; Jiang, W.Y. Exploration breakthroughs and geological characteristics of continental shale oil: A case study of the Kongdian Formation in the Cangdong Sag, China. *Mar. Petrol. Geol.* **2019**, *102*, 544–556. [CrossRef]
20. Stow, D.A.V.; Bowen, A.J. Origin of lamination in deep sea, fine-grained sediments. *Nature* **1978**, *274*, 324–328. [CrossRef]
21. Macquaker, J.H.S.; Adams, A.E. Maximizing Information from Fine-Grained Sedimentary Rocks: An Inclusive Nomenclature for Mudstones. *J. Sediment. Res.* **2003**, *73*, 735–744. [CrossRef]
22. Li, W.; Lu, S.; Xue, H.; Zhang, P.; Hu, Y. Oil content in argillaceous dolomite from the Jianghan Basin, China: Application of new grading evaluation criteria to study shale oil potential. *Fuel* **2015**, *143*, 424–429. [CrossRef]
23. Li, Q.; Chen, F.; Wu, S.; Zhang, L.; Wang, Y.; Xu, S. A simple and effective evaluation method for lacustrine shale oil based on mass balance calculation of Rock-Eval data. *Appl. Geochem.* **2022**, *140*, 105287. [CrossRef]
24. Li, Q.; Xu, S.; Hao, F.; Shu, Z.; Chen, F.; Lu, Y.; Wu, S.; Zhang, L. Geochemical characteristics and organic matter accumulation of argillaceous dolomite in a saline lacustrine basin: A case study from the paleogene xingouzui formation, Jianghan Basin, China. *Mar. Petrol. Geol.* **2021**, *128*, 105041. [CrossRef]
25. Li, W.; Lu, S.; Xue, H.; Zhang, P.; Wu, S. The formation environment and developmental models of argillaceous dolomite in the Xingouzui Formation, the Jianghan Basin. *Mar. Petrol. Geol.* **2015**, *67*, 692–700. [CrossRef]
26. Li, W.; Wang, W.; Lu, S.; Xue, H. Quantitative characterization on shale-hosted oil reservoir: A case study of argillaceous dolomite reservoir in the Jianghan Basin. *Fuel* **2017**, *206*, 690–700. [CrossRef]
27. Zhang, P.; Lu, S.; Li, J.; Xue, H.; Li, W.; Zhang, P. Characterization of shale pore system: A case study of Paleogene Xin'gouzui Formation in the Jianghan basin, China. *Mar. Petrol. Geol.* **2017**, *79*, 321–334. [CrossRef]
28. Huang, C.; Hinnov, L. Evolution of an Eocene-Oligocene saline lake depositional system and its controlling factors, Jianghan Basin, China. *J. Earth Sci. China* **2014**, *25*, 959–976. [CrossRef]
29. Wu, L.; Mei, L.; Liu, Y.; Luo, J.; Min, C.; Lu, S.; Li, M.; Guo, L. Multiple provenance of rift sediments in the composite basin-mountain system: Constraints from detrital zircon U-Pb geochronology and heavy minerals of the early Eocene Jianghan Basin, central China. *Sediment. Geol.* **2017**, *349*, 46–61. [CrossRef]
30. Wu, L.; Mei, L.; Liu, Y.; Paton, D.A.; Luo, J.; Yu, L.; Wang, D.; Min, C.; Li, M.; Guo, L.; et al. The stratigraphic and structural record of the Cretaceous Jianghan Basin, central China: Implications for initial rifting processes and geodynamics. *Cretac. Res.* **2018**, *90*, 21–39. [CrossRef]
31. Peng, W. Deposition and distribution characteristics of beach-bar sand in the lower member of Xingouzui Formation in Jianghan Basin. *J. Yangtze Univ. Nat. Sci. Ed.* **2019**, *16*, 9–15. (In Chinese with English abstract).
32. Huang, C.; Hinnov, L. Astronomically forced climate evolution in a saline lake record of the middle Eocene to Oligocene, Jianghan Basin, China. *Earth Planet. Sci. Lett.* **2019**, *528*, 115846. [CrossRef]
33. Li, Q.; Xu, S.; Zhang, L.; Chen, F.; Wu, S.; Bai, N. Shale Oil Enrichment Mechanism of the Paleogene Xingouzui Formation, Jianghan Basin, China. *Energies* **2022**, *15*, 4038. [CrossRef]
34. Gou, Q.; Xu, S.; Hao, F.; Yang, F.; Zhang, B.; Shu, Z.; Zhang, A.; Wang, Y.; Lu, Y.; Cheng, X. Full-scale pores and micro-fractures characterization using FE-SEM, gas adsorption, nano-CT and micro-CT: A case study of the Silurian Longmaxi Formation shale in the Fuling area, Sichuan Basin, China. *Fuel* **2019**, *253*, 167–179. [CrossRef]
35. Gou, Q.; Xu, S.; Hao, F.; Yang, F.; Shu, Z.; Liu, R. The effect of tectonic deformation and preservation condition on the shale pore structure using adsorption-based textural quantification and 3D image observation. *Energy* **2021**, *219*, 119579. [CrossRef]
36. Teng, X.; Wang, C.; Liu, C.; Yan, K.; Luo, Z. Paleocene-Eocene Thermal Maximum lacustrine sediments in deep drill core SKD1 in the Jianghan Basin: A record of enhanced precipitation in central China. *Glob. Planet Chang.* **2021**, *205*, 103620. [CrossRef]
37. Chen, Z.; Wang, X.; Hu, J.; Yang, S.; Zhu, M.; Dong, X.; Tang, Z.; Peng, P.; Ding, Z. Structure of the carbon isotope excursion in a high-resolution lacustrine paleocene–eocene thermal maximum record from central china. *Earth Planet. Sci. Lett.* **2014**, *408*, 331–340. [CrossRef]
38. Peters, K.E. Guidelines for evaluating petroleum source rock using programmed pyrolysis. *AAPG Bull.* **1986**, *70*, 318–329.
39. Creaney, S.; Passey, Q.R. Recurring patterns of total organic carbon and source rock quality within a sequence stratigraphic framework. *AAPG Bull.* **1993**, *77*, 386–401.
40. Du, X.; Liu, X.; Lu, Y.; Liu, H.; Zhang, P.; Ma, Y.; Zhao, K.; Wei, W. Characteristics and development models of continental fine-grained mixed sedimentation: A case study of Dongying sag. *Acta Pet. Sin.* **2022**, *41*, 1324–1333. (In Chinese with English abstract).
41. Zhang, J.; Pas, D.; Krijgsman, W.; Wei, W.; Du, X.; Zhang, C.; Liu, J.; Lu, Y. Astronomical forcing of the paleogene coal-bearing hydrocarbon source rocks of the east china sea shelf basin. *Sediment. Geol.* **2020**, *406*, 105715.
42. Jin, Z.; Zhu, R.; Liang, X.; Shen, Y. Several issues worthy of attention in current lacustrine shale oil exploration and development. *Pet. Explor. Dev.* **2021**, *48*, 14. [CrossRef]
43. Dahl, T.W.; Ruhl, M.; Hammarlund, E.U.; Canfield, D.E.; Rosing, M.T.; Bjerrum, C.J. Tracing euxinia by molybdenum concentrations in sediments using handheld X-ray fluorescence spectroscopy (HHXRF). *Chem. Geol.* **2013**, *360–361*, 241–251. [CrossRef]
44. Lu, Y.; Huang, C.; Jiang, S.; Zhang, J.; Lu, Y.; Liu, Y. Cyclic late Katian through Hirnantian glacioeustasy and its control of the development of the organic-rich Wufeng and Longmaxi shales, South China. *Palaeogeogr. Palaeoclimatol. Palaeoecol.* **2019**, *526*, 96–109. [CrossRef]
45. Shi, J.; Jin, Z.; Liu, Q.; Huang, Z.; Hao, Y. Terrestrial sedimentary responses to astronomically forced climate changes during the Early Paleogene in the Bohai Bay Basin, eastern China. *Palaeogeogr. Palaeoclimatol. Palaeoecol.* **2018**, *502*, 1–12. [CrossRef]

46. Yang, H.; Huang, Y.; Ma, C.; Zhang, Z.; Wang, C. Recognition of Milankovitch cycles in XRF core-scanning records of the Late Cretaceous Nenjiang Formation from the Songliao Basin (northeastern China) and their paleoclimate implications. *J. Asian Earth Sci.* **2020**, *194*, 104183. [CrossRef]
47. Li, Y.; Shao, D.; Lv, H.; Zhang, Y.; Zhang, X.; Zhang, T. Relationship between elemental geochemical characteristics and organic matter enrichment in marine shale of Wufeng Formation-Longmaxi Formation, Sichuan Basin. *Acta Pet. Sin.* **2015**, *12*, 1470–1483. (In Chinese with English abstract).
48. Raiswell, R.; Buckley, F.; Berner, R.A.; Anderson, T.F. Degree of pyritization of iron as a paleoenvironmental indicator of bottom-water oxygenation. *J. Sediment. Petrol.* **1988**, *58*, 812–819.
49. Algeo, T.J.; Jiangsi, L. A re-assessment of elemental proxies for paleoredox analysis. *Chem. Geol.* **2020**, *540*, 119549. [CrossRef]
50. Slatt, R.M.; Rodriguez, N.D. Comparative sequence stratigraphy and organic geochemistry of gas shales: Commonality or coincidence? *J. Nat. Gas Sci. Eng.* **2012**, *8*, 68–84. [CrossRef]
51. Chen, C.; Jiang, Z.; Kong, X.; Wu, S.; Chen, F.; Yang, Y. Sedimentary characteristics of intersalt fine-grained sedimentary rocks and their control on oil-bearing ability of shales in the Qianjiang Formation, Qianjiang Sag. *Earth Sci. Front.* **2021**, *28*, 421–435. (In Chinese with English abstract).
52. Wei, W.; Algeo, T.J. Elemental proxies for paleosalinity analysis of ancient shales and mudrocks. *Geochim. Cosmochim. Acta* **2020**, *287*, 341–366. [CrossRef]
53. Cramwinckel, M.J.; Huber, M.; Kocken, I.J.; Agnini, C.; Bijl, P.K.; Bohaty, S.M.; Frieling, J.; Goldner, A.; Hilgen, F.J.; Kip, E.L.; et al. Synchronous tropical and polar temperature evolution in the Eocene. *Nature* **2018**, *559*, 382–386. [CrossRef] [PubMed]
54. Zachos, J.C.; Dickens, G.R.; Zeebe, R.E. An early Cenozoic perspective on greenhouse warming and carbon-cycle dynamics. *Nature* **2008**, *451*, 279–283. [CrossRef]
55. Zachos, J.; Pagani, M.; Sloan, L.; Thomas, E.; Billups, K. Trends, Rhythms, and Aberrations in Global Climate 65 Ma to Present. *Science* **2001**, *292*, 686–693. [CrossRef]
56. Kennett, J.P.; Stott, L.D. Abrupt deep-sea warming, palaeoceanographic changes and benthic extinctions at the end of the Palaeocene. *Nature* **1991**, *353*, 225–229. [CrossRef]
57. Xie, Y.; Wu, F.; Fang, X. A transient south subtropical forest ecosystem in central China driven by rapid global warming during the Paleocene-Eocene Thermal Maximum. *Gondwana Res.* **2022**, *101*, 192–202. [CrossRef]
58. Chen, Z. Carbon-cycle dynamics during the Paleocene-Eocene Thermal Maximum. *Chin. Sci. Bull.* **2021**. (In Chinese with English abstract). [CrossRef]
59. Xu, L.; Yan, C.; Yu, H.; Wang, B.; Yu, F.; Wang, D. Chronology of Paleogene volcanic rocks in the Jianghan Basin. *Oil Gas Geol.* **1995**, *16*, 132–137. (In Chinese with English abstract).
60. Teng, X.; Fang, X.; Kaufman, A.J.; Liu, C.; Wang, J.; Zan, J.; Yang, Y.; Wang, C.; Xu, H.; Schulte, R.F.; et al. Sedimentological and mineralogical records from drill core SKD1 in the Jianghan Basin, Central China, and their implications for late Cretaceous–early Eocene climate change. *J. Asian Earth Sci.* **2019**, *182*, 103936. [CrossRef]
61. Yang, H.; Zhao, Y.; Cui, Q.; Ren, W.; Li, Q. Paleoclimatic indication of X-ray fluorescence core-scanned Rb/Sr ratios: A case study in the Zoige Basin in the eastern Tibetan Plateau. *Sci. China Earth Sci.* **2020**, *64*, 80–95. [CrossRef]